Rapid Robust Design of a Deployable System for Boost-Glide Vehicles

Bradley A. Steinfeldt*, Grant A. Rossman*, Robert D. Braun†
Georgia Institute of Technology, Atlanta, GA 30332
and
Gregg H. Barton‡
C. S. Draper Laboratory, Inc., Houston, TX 77058

Deployable devices have the potential to reduce or eliminate physical constraints placed on vehicle design while enhancing the aerodynamics characteristics of the system. This investigation looks at augmenting an existing boost-glide system with a deployable device to increase the system's range or accuracy by varying design parameters. Two different configurations are considered, one which has a single-delta shape and one with a double-delta. A rapid robust design methodology that views the multidisciplinary design problem as a dynamical system is implemented to robustly design the deployable. This methodology allows concepts from dynamical system theory to be used in order to broaden the computational tools available to the MDO problem. In addition to the physical parameters of the deployable device, the impact of the guidance algorithm is also considered. The product of this investigation is a family of designs which compare favorably to those obtained through traditional Monte Carlo methods and are achievable in less than 5% of the computational time. The obtained deployable designs have the capability to enhance the baseline boost-glide system's 1σ range by 50% and improve the 1σ accuracy by an order of magnitude. It is seen that the single-delta configuration provides similar accuracy as the double-delta; however, the double-delta configuration is capable of providing ranges that are twice that of the single-delta.

Nomenclature

$\bar{(\cdot)}$	Mean value of $(\cdot)$
β	Ballistic coefficient
$\boldsymbol{\beta}$	Deterministic input contribution in the fixed-point iteration equation, $\boldsymbol{\beta} \in \mathbb{R}^{m\times d}$
$\boldsymbol{\delta}$	Bias in the fixed-point iteration equation, $\boldsymbol{\delta} \in \mathbb{R}^{m}$
$\boldsymbol{\gamma}$	Probabilistic input contribution in the fixed-point iteration equation, $\boldsymbol{\gamma} \in \mathbb{R}^{m\times p}$
$\boldsymbol{\Lambda}$	State contribution in the fixed-point iteration equation, $\boldsymbol{\Lambda} \in \mathbb{R}^{m\times m}$
$\boldsymbol{\Sigma}$	Covariance matrix
ϵ	Convergence tolerance
$\mathbf{1}_q$	A $1 \times q$ vector of ones
$\mathbf{A_j}$	Matrix describing the state contribution of the j^{th} contributing analysis, $\mathbf{A_j} \in \mathbb{R}^{l_j\times m}$
$\mathbf{B_j}$	Matrix describing the deterministic input contribution of the j^{th} contributing analysis, $\mathbf{B_j} \in \mathbb{R}^{l_j\times d}$
$\mathbf{C_j}$	Matrix describing the probabilistic input contribution of the j^{th} contributing analysis, $\mathbf{C_j} \in \mathbb{R}^{l_j\times p}$
$\mathbf{d_j}$	Bias associated with the j^{th} contributing analysis, $\mathbf{d_j} \in \mathbb{R}^{l_j}$
$\mathbf{L_{BA}}$	Transformation matrix from frame $\mathcal{B}$ to frame $\mathcal{A}$

*Graduate Research Assistant, Guggenheim School of Aerospace Engineering, AIAA Student Member
†David and Andrew Lewis Professor of Space Technology, Guggenheim School of Aerospace Engineering, AIAA Fellow
‡Principal Member of Technical Staff, AIAA Senior Member

$\mathbf{N}$	Matrix multiplying the pertinent contributing analyses outputs to the design's response in the Taylor series expansion of the response function, $\mathbf{N} \in \mathbb{R}^{1\times q}$
$\mathbf{r}$	Radius vector
$\mathbf{u_d}$	Deterministic system-level inputs into the design, $\mathbf{u_d} \in \mathbb{R}^d$
$\mathbf{u_p}$	Probabilistic system-level inputs into the design, $\mathbf{u_d} \in \mathbb{R}^d$
$\mathbf{y_j}$	Contributing analysis output, $\mathbf{y_j} \in \mathbb{R}^{l_j}$
$\mathcal{I}$	Inertial frame
μ_g	Gravitational parameter
ν	Poisson's ratio
ϕ	Longitude
ψ	Heading angle
ρ	Atmospheric density
σ	Bank angle
σ_t	Material tensile strength
θ	Latitude
$\tilde{(\cdot)}$	Nominal value of $(\cdot)$
A	Area
a	Ellipsoid semi-major axis
b	Ellipsoid semi-minor axis
C_D	Drag coefficient
C_L	Lift coefficient
E	Young's modulus
g	Magnitude of the acceleration due to gravity
H	Atmospheric scale height
h	Altitude
k_s	Sutton-Graves constant
k_{C_D}	Drag coefficient multiplier
k_{C_L}	Lift coefficient multiplier
L/D	Lift-to-drag ratio
l/d	Deployable length to vehicle diameter ratio
m	Mass
p	Deployable internal pressure
Q	Integrated heat load
r_n	Stagnation radius
v	Velocity magnitude
z	Ellipsoid altitude

Subscripts

0	Initial value
nom	Nominal value
T	Target value
baseline	Reference to the baseline strategic system

I. Background

As the demands on the performance of entry, descent, and landing (EDL) systems increase, additional technologies will be needed in order to enable the desired mission sets. Deployable devices are one such technology, which reduce or eliminate the maximum diameter constraint placed on the entry vehicle shape by the launch or boost vehicle, allowing the system to have more favorable aerodynamics. Relaxation or elimination of this constraint gives the potential to enable a broad spectrum of next-generation missions for both NASA and national defense applications. Some examples of previously investigated deployable systems are discussed in Refs. 1–15.

Boost-glide systems are typically mid- to high-L/D systems that use a boost phase to achieve a desired state and then manage their energy to glide to their desired target. Deployables are usually thought to be drag enhancing devices to reduce the ballistic coefficient of a system. However, for boost-glide vehicles, the inclusion of a deployable device may also improve controllability, enhance constraint margins, and lead to

new concepts of operations. In addition to new boost-glide systems, deployables could be added to existing strategic systems leading to an evolved boost-glide mission set through increased range and accuracy.

This work robustly designs deployable systems for a representative existing strategic system in order to examine this evolved boost-glide mission set. A novel rapid robust design methodology is employed in the design process which exploits the synergy between multidisciplinary design and dynamical systems to rapidly explore the design space in light of uncertainties. The results are then compared to a traditional robust design technique.

II. Performance Impact of a Deployable System

In general, the performance of a vehicle is strongly characterized by two parameters, the ballistic coefficient, β, defined as

$$\beta = \frac{m}{C_D A} \tag{1}$$

and the lift-to-drag ratio, L/D.[16] Figure 1 show the 1σ miss distance to a target on the ground and achievable range for an arbitrary system as a function of these two parameters.

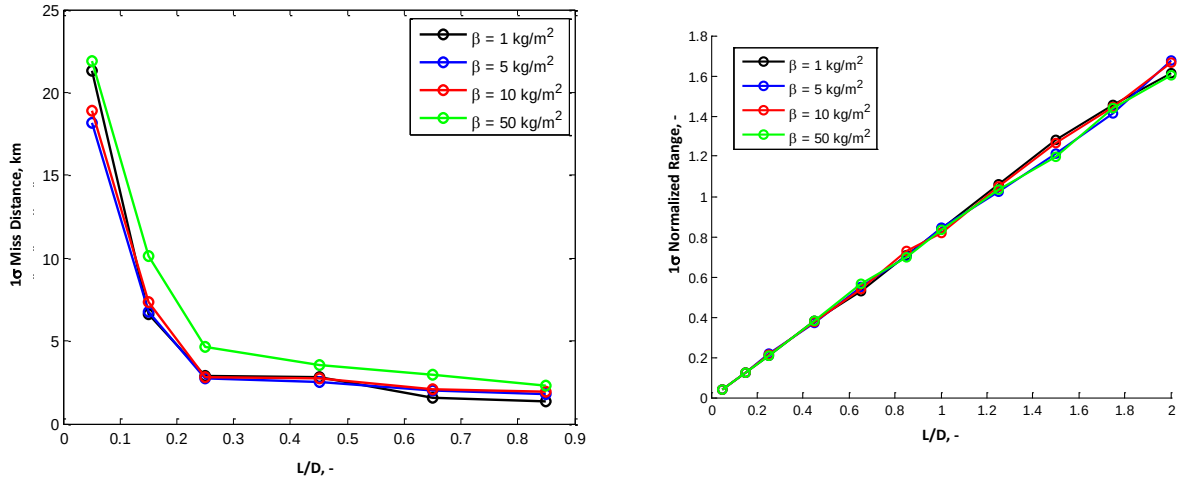

(a) (b)

Figure 1. Variation of (a) miss distance and (b) with ballistic coefficient and lift-to-drag ratio.

The results seen in Fig. 1 are the product of solving the optimal control problem where the control is the orientation and magnitude of the net aerodynamic force (or acceleration) vector. It was assumed that the aerodynamic force vector could be oriented freely and non-continuously within a reachable cone having a half-angle defined by the maximum L/D. The objective function to be maximized for this optimization problem is that either the accuracy (in the case of Fig. 1(a)) or range (in the case of Fig. 1(b)) is maximized.

In Fig. 1, it is seen that the miss distance is relatively insensitive to ballistic coefficient; however, there is a strong, nonlinear dependence on L/D for values less than 0.3 with results being approximately linear beyond this point. A strong, near-linear dependence on L/D is seen for the range of the system. However, like with the accuracy, there is little sensitivity to the ballistic coefficient.

There is a large design space of deployable decelerator concepts, therefore, this application will limit the design to a single decelerator concept—that of deployable chines, which as shown in Fig. 2 have the potential to increase the L/D performance of the system. In this figure, the improvement over a representative baseline's L/D is plotted against a non-dimensional size, l/d—the ratio of the distance from the centerline of the vehicle of the trailing edge of the deployable to the baseline vehicle's diameter. Figure 1 implies that from a performance perspective, the vehicle should have as much L/D as possible while Fig. 2 indicates that in order to maximize the L/D of the system, the deployable should be as large as possible. Indeed, from the performance side this is true; however, the larger the deployable the more massive it is, which negatively impacts the performance of the system. Therefore a multiobjective design problem is formulated where the mass of the decelerator is traded with the performance of the system (either accuracy or range).

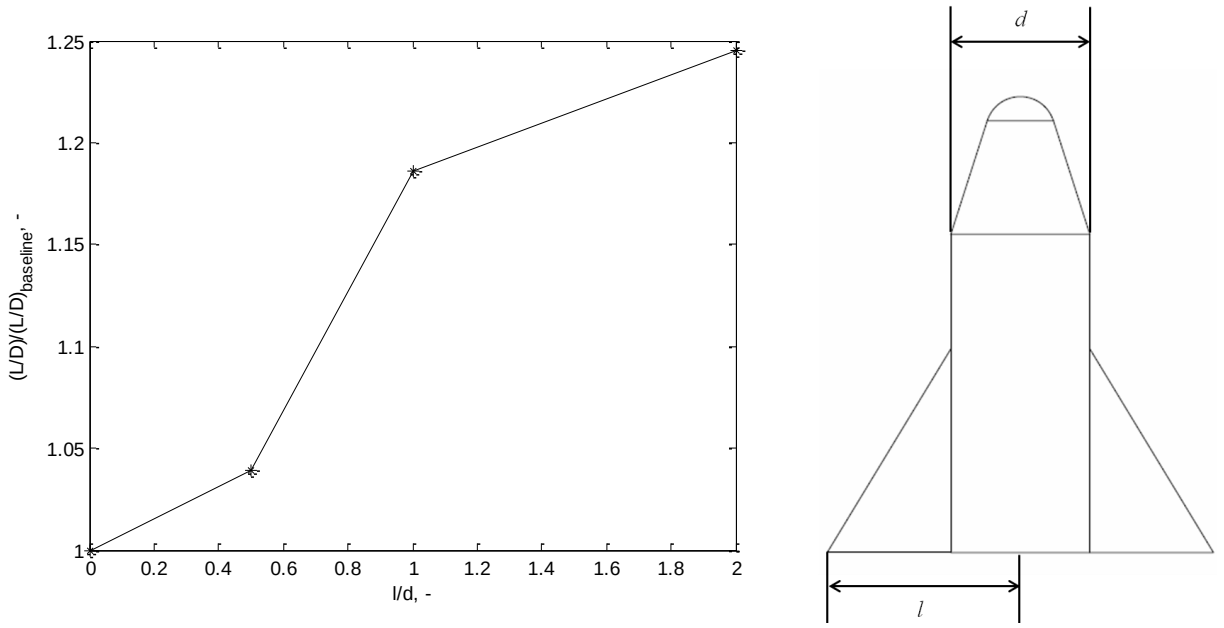

Figure 2. Increase in the maximum lift-to-drag ratio of the entry system for a single-delta deployable as a function of deployable size.

III. A Rapid Robust Multidisciplinary Design Methodology

In Refs. 17 and 18, a methodology that rapidly obtains the mean and a bound on the variance of a multidisciplinary design was developed. This new methodology is possible by viewing the multidisciplinary design problem as a dynamical system. In fact, two dynamical systems are formed, both of which are root-finding problems. The first dynamical system addresses the identification of feasible designs through the enforcement of compatibility constraints. For this system, the state is the contributing analyses (CAs) output. The second dynamical system formed is that of finding an optimum of the design, where the state is the objective function of the optimization.

Viewing the multidisciplinary design problem as a dynamical system, enables techniques to be brought from one field into another. In particular, stability, control, and estimation techniques from dynamical system theory are applied in order to rapidly obtain a robust optimal design.[17] In addition, two additional techniques from non-traditional design fields are also used in this methodology, the unscented transform and the matrix 2-norm. The unscented transform, exploits the eigenstructure to obtain third-order accurate statistical information about nonlinear systems.[19] The matrix 2-norm provides a conservative bound for the output covariance variance, as it finds the principal eigenvalue (*i.e.*, the "variance" along the principal direction of the covariance matrix). This quantity gives a bound on the variance and can be used as a direct surrogate for the variance for fixed distributions as the observed error remains identical.

III.A. Procedure

The robust design procedure implemented in this work is outlined below following that outlined in Ref. 17 and its notation.

Step 1: Decompose the Design
A general multidisciplinary design can be decomposed into multiple CAs. Each of these CAs represents an analysis that contributes to the entire design. In the theoretical development underlying Ref. 17, it is assumed that each of the n CAs are linear and algebraic, where the output of each of the CAs is of the form

$$\mathbf{y_j} = \mathbf{A_j y} + \mathbf{B_j u_d} + \mathbf{C_j u_p} + \mathbf{d_j} \tag{2}$$

where $\mathbf{y_j} \in \mathbb{R}^{l_j}$, $\mathbf{y} \in \mathbb{R}^m$ is the concatenated output from all of the CAs, $\mathbf{u_d} \in \mathbb{R}^d$ are the deterministic system-level inputs into the design, $\mathbf{u_p} \in \mathbb{R}^p$ are the probabilistic system-level inputs into the design, and

$\mathbf{d_j} \in \mathbb{R}^{l_j}$ is the bias associated with the model. This implies $\mathbf{A_j} \in \mathbb{R}^{l_j \times m}$, $\mathbf{B_j} \in \mathbb{R}^{l_j \times d}$, $\mathbf{C_j} \in \mathbb{R}^{l_j \times p}$, and that $\sum_{j=1}^{n} l_j = m$.

For general designs where the CAs may not be linear, the required functional form can be achieved through linearization where $\mathbf{A_j} = \left.\frac{\partial \mathbf{g}}{\partial \mathbf{y}}\right|_{\tilde{\mathbf{y}}}$, $\mathbf{B_j} = \left.\frac{\partial \mathbf{g}}{\partial \mathbf{u_d}}\right|_{\tilde{\mathbf{u}}_\mathbf{d}}$, $\mathbf{C_j} = \left.\frac{\partial \mathbf{g}}{\partial \mathbf{u_p}}\right|_{\tilde{\mathbf{u}}_\mathbf{p}}$, and

$$\mathbf{d_j} = -\left(\mathbf{A_j}\tilde{\mathbf{y}} + \mathbf{B_j}\tilde{\mathbf{u}}_\mathbf{d} + \mathbf{C_j}\tilde{\mathbf{u}}_\mathbf{p}\right)$$

when the input-output relationship for the CA is given by $\mathbf{y_j} = \mathbf{g}\left(\mathbf{y}, \mathbf{u_d}, \mathbf{u_p}\right)$ and $\tilde{(\cdot)}$ is the value of $(\cdot)$ about which the function is linearized.

Step 2: Identify the Random Variables and their Distributions
In order to propagate these uncertainties through the design to estimate the robustness, the probabilistic variables must be identified. The random variables associated with the uncertainty within the design are handled in two different ways depending on where the random variable is functionally located. Functionally, the uncertainty resulting from inputs into the design refers to uncertainties associated with $\mathbf{u_p}$, whereas uncertainty associated with the physical modeling pertain to $\mathbf{A_j}$, $\mathbf{B_j}$, $\mathbf{C_j}$, or $\mathbf{d_j}$. In the first instance, the mean is propagated in the $\hat{\mathbf{y}}_{k|k}$ term of the filter equations and the covariance is propagated in the $\mathbf{\Sigma}_{k|k}$ term of the filter equations. In the second case, the mean is again accounted for in the $\hat{\mathbf{y}}_{k|k}$ term of the equations; however, the covariance is accounted for in the $\mathbf{Q}_k$ term of the filter.

Step 3: Form the Iterative Equations
In order to implement the discrete Kalman filter, a causal, discrete dynamical system must be formed. The process of converging the multidisciplinary design through root. Assuming fixed-point iteration is used to converge the design, the dynamical system is given by

$$\mathbf{y}_k = \mathbf{\Lambda}\mathbf{y}_{k-1} + \boldsymbol{\beta}\mathbf{u_d} + \boldsymbol{\gamma}\mathbf{u_p} + \boldsymbol{\delta} \tag{3}$$

where it is assumed that $\mathbf{\Lambda} = \begin{pmatrix} \mathbf{A_1} \\ \vdots \\ \mathbf{A_n} \end{pmatrix} \in \mathbb{R}^{m \times m}$, $\boldsymbol{\beta} = \begin{pmatrix} \mathbf{B_1} \\ \vdots \\ \mathbf{B_n} \end{pmatrix} \in \mathbb{R}^{m \times d}$, $\boldsymbol{\gamma} = \begin{pmatrix} \mathbf{C_1} \\ \vdots \\ \mathbf{C_n} \end{pmatrix} \in \mathbb{R}^{m \times p}$, and $\boldsymbol{\delta} = \begin{pmatrix} \mathbf{d_1} \\ \vdots \\ \mathbf{d_n} \end{pmatrix} \in \mathbb{R}^{m}$.

Step 4: Ensure a Solution Exists
Since the iterative system defined by Eq. (3) is a discrete, linear, dynamical system, the existence of a solution to the multidisciplinary design problem is given solely by the stability of the system. In particular, if the system is asymptotically stable, a converged design exists for some initial guess of the CA outputs and if it is globally asymptotically stable, a design exists for all initial guesses of the CA outputs.

Since this problem is inherently nonlinear, a Lyapunov function technique can be used to investigate the stability (and convergence) of the design. In this case, for asymptotic stability, a positive-definite function is sought whose difference between iterates in some region around the origin is negative definite. The search for a Lyapunov function can be accomplished using several methods, including some numerical based techniques (see Refs. 18, 20, and 21).

Step 5: Estimate the Mean Output and the Covariance
The mean output of the multidisciplinary system and the associated covariance matrix are found by propagating the Kalman filter equations until convergence. In order to accomplish this, the iterative system formed in Eq. (3) needs to be transformed to the form needed in Kalman filter. This is a relatively straightforward process when the following substitutions are made

$$\mathbf{F}_{k-1} = \mathbf{\Lambda}, \quad \forall k \in \{1, 2, ..., n\} \tag{4}$$

$$\mathbf{B}_{k-1} = \begin{pmatrix} \boldsymbol{\beta} & \boldsymbol{\gamma} & \mathbf{I_{m\times m}} \end{pmatrix}, \quad \forall k \in \{1, 2, ..., n\} \tag{5}$$

$$\mathbf{u}_{k-1} = \begin{pmatrix} \mathbf{u_d} \\ \mathbf{u_p} \\ \boldsymbol{\delta} \end{pmatrix}, \quad \forall k \in \{1, 2, ..., n\} \tag{6}$$

The mean state, that is the output of the analyses, ($\hat{\mathbf{y}}_{0|0}$) and the covariance matrix associated with the state ($\mathbf{\Sigma}_{0|0}$) are initialized by the relations

$$\hat{\mathbf{y}}_{0|0} = \mathbf{y_0} \tag{7}$$

$$\mathbf{\Sigma}_{0|0} = \mathbf{\Sigma_0} \tag{8}$$

where $\mathbf{y_0}$ and $\mathbf{\Sigma_0}$ are found by assuming a starting value for the coupled CA and an input covariance matrix associated with the parameters of the problem. These values are then propagated through each CA of a serial (*i.e.*, uncoupled) design structure matrix using the unscented transform technique. The concatenated output of each of the CAs is then used to form $\mathbf{y_0}$ and the covariance matrix $\mathbf{\Sigma_0}$, which will initially be a block diagonal matrix. The last parameter which need to be identified in order to estimate the mean output and the covariance of the system is the covariance matrix associated with the model, $\mathbf{Q}$. This is a block diagonal matrix composed of the variances and covariances associated with $\mathbf{A_j}$, $\mathbf{B_j}$, $\mathbf{C_j}$, and $\mathbf{d_j}$.

The iterates are then found by by propagating the filter equations with $\mathbf{H}_{k-1} = \mathbf{I_{m\times m}} \quad \forall k \in \{1, 2, ..., n\}$ and $\mathbf{R}_{k-1} = \mathbf{0} \quad \forall k \in \{1, 2, ..., n\}$ until the design convergence criterion is met. The exact convergence criterion can be of several forms, the two criterion used within this work are an absolute tolerance of the state and a relative tolerance of the state. These are demonstrated in the following relations

$$\| \hat{\mathbf{y}}_{k|k} - \hat{\mathbf{y}}_{k-1|k-1} \|_2 \leq \epsilon_1 \tag{9}$$

$$\frac{\| \hat{\mathbf{y}}_{k|k} - \hat{\mathbf{y}}_{k-1|k-1} \|_2}{\| \hat{\mathbf{y}}_{k-1|k-1} \|_2} \leq \epsilon_2 \tag{10}$$

Step 6: Identify the Mean and Variance Bound of the Objective Function
Assuming that the design objective (*e.g.*, the 1σ accuracy or 1σ range) is the result of a first-order expansion of an objective function that is of the form

$$r = g(\mathbf{y}^*) \tag{11}$$

The linearized objective function, Eq. (11), about $\mathbf{y^*_{nom}}$ is then given by

$$\tilde{r} = \frac{\partial g}{\partial \mathbf{y}^*}\mathbf{y}^* - \frac{\partial g}{\partial \mathbf{y}^*}\mathbf{y^*_{nom}} = \mathbf{N}\mathbf{y}^* + b \tag{12}$$

which leads to the results

$$\bar{r} \approx \mathbf{N}\hat{\mathbf{y}}^*_{n|n} + b \tag{13}$$

$$\sigma_r^2 \approx \| \mathbf{\Sigma}_{\boldsymbol{y^*}_{n|n}} \|_2 \, \mathbf{N}\mathbf{1}_q^T \tag{14}$$

where it is assumed that $\mathbf{N} \in \mathbb{R}^{1\times q}$.

Step 7: Optimize for Uncertainty and Ensure Constraints are Met
Formulating the output of Step 6 in terms of the mean and variance allows for an optimal control problem to be setup where the objective function is defined by

$$\mathcal{J} = \mathbf{N}\left(\alpha\hat{\mathbf{y}}^*_{n|n} + \beta \| \mathbf{\Sigma}_{\boldsymbol{y^*_{n|n}}} \|_2 \, \mathbf{1}_q^T\right) \tag{15}$$

and α and β are weights on the relative components that can be varied to find different compromised optimal designs. The problem is then to seek out the control, $\mathbf{u}$, that minimizes $\mathcal{J}$. In this case the control is constant (since they are parameters of the problem) and given by $\mathbf{u_d}$. The requirements outside of the compatibility constraints are then handled by adjoining the set of convex constraints to the objective function and identifying an optimum that satisfies the necessary conditions outlined previously.

Step 8: Evaluate the Quality of the Robustness Estimate
The quality of the robustness estimate can be evaluated by using the unscented transform to get a higher-order estimate of the mean and the covariance of the output. The procedure to obtain this estimate is as follows:

1. Identify the uncertain parameters for the problem and form the initial covariance matrix for these parameters
2. Identify the m (or $m+1$ if an alternate form of the unscented transform is used) sigma points based on the eigenstructure of the initial covariance matrix
3. Propagate each of these sigma points through the design until convergence
4. Record the objective function for each sigma point propagation
5. Compute the scalar mean and variance from the composite results for each of the objective function values

IV. Baseline Strategic System Characteristics

The rapid robust design methodology is used to design a deployable system that could be added to a representative baseline strategic system to potentially improve its performance. The baseline system is shown in Fig. 3 along with selected characteristics describing its aerodynamics. It is assumed that the mass of the system, m_{baseline}, is 5,000 kg.

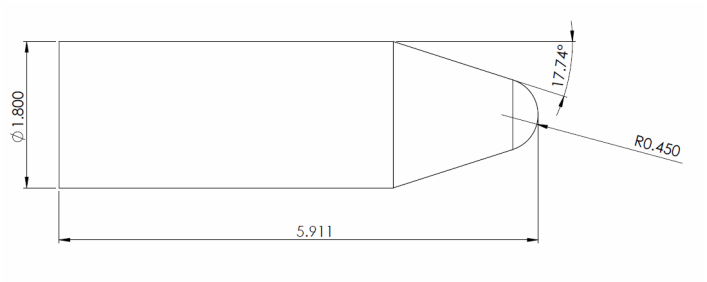

Parameter	Value
$(L/D)_{\max}$	1.02
$\alpha\|_{(L/D)_{\max}}$	22.5°
$C_L\|_{(L/D)_{\max}}$	0.864
$C_D\|_{(L/D)_{\max}}$	0.849

Figure 3. Baseline strategic vehicle characteristics.

V. Modeling

This design can be decomposed into seven CAs as shown in Fig. 4. In the discussion that follows, the models for each of these CAs will be discussed.

V.A. Planetary Model

This analysis assumes an inverse square law gravity field as shown in Eq. (16)

$$\mathbf{a_g} = -\frac{\mu_g}{r^3}\mathbf{r} \tag{16}$$

where μ_g is the gravitational parameter. The magnitude of the gravitational acceleration is

$$g = \| \mathbf{a_g} \| = \frac{\mu_g}{r^2} \tag{17}$$

In addition, an exponential atmospheric density profile given by

$$\rho(h) = \rho_0 \exp\left(-\frac{h}{H}\right) \tag{18}$$

was used.

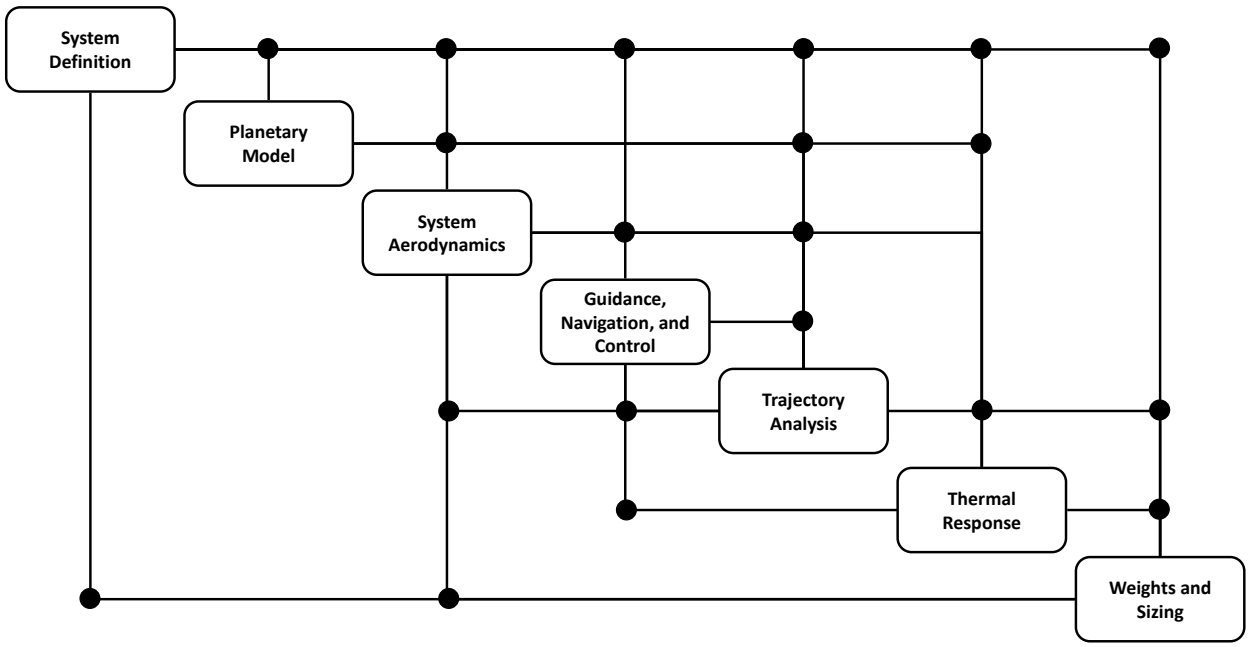

Figure 4. Design structure matrix for the design of a deployable for a strategic system.

V.B. System Aerodynamics

For this investigation, a hypersonic aerodynamics analysis of the baseline strategic system along with the deployable was performed using a Newtonian impact model. These results were generated with a first-order industry standard tool, the configuration based aerodynamics (CBAero) tool.[22] The conditions at the maximum lift-to-drag ratio, $(L/D)_{\max}$, were then regressed as a function of the size of the deployable (*e.g.*, $C_L(l/d)$, $C_D(l/d)$, etc.) for use in the design of the deployable system. The deployable is assumed to be a single-delta shape as shown in Fig. 5.

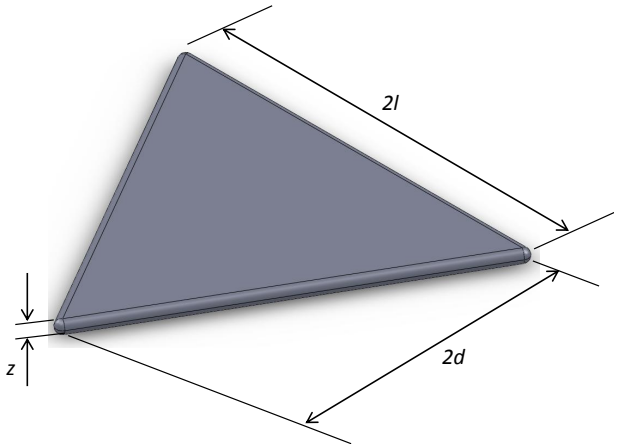

Figure 5. Geometry of the deployable device.

V.C. Guidance, Navigation, and Control

Two different guidance schemes are considered in this work: bank-to-steer guidance and acceleration control.

V.C.1. Bank-to-Steer Guidance

Bank-to-steer guidance has been used on missions such as Apollo and the Mars Science Laboratory.[23,24] This control technique rotates the lift vector around the velocity vector. In the downrange direction, control is provided by varying the amount of vertical lift, which is proportional to the cosine of the bank angle, (*i.e.*, $(L/D)_{vert} \sim \cos(\sigma)$). Crossrange control is controlled by bank reversals since both σ and $-\sigma$ provide the same $(L/D)_{vert}$.

V.C.2. Acceleration Control

Acceleration control is a bounding technique which controls the direction of the aerodynamic acceleration vector assuming that the maximum acceleration obtainable is equal to that of the maximum acceleration due to drag. The direction of the acceleration vector is allowed to freely vary within a cone with half-angle θ_c defined by the lift-to-drag ratio of the system

$$\theta_c = \tan^{-1}\left(\frac{L}{D}\right) = \tan^{-1}\left(\frac{C_L}{C_D}\right) \tag{19}$$

Mathematically the commanded acceleration is given by

$$\mathbf{a_c} = \frac{D_{\max}}{m}\hat{\mathbf{u}} = \frac{\rho v^2 C_D|_{\alpha=0^\circ} A}{2m}\frac{\mathbf{u}}{\parallel \mathbf{u} \parallel} \tag{20}$$

with the constraint that

$$\cos^{-1}\left(\frac{\hat{\mathbf{u}}^T\mathbf{v}}{v}\right) \leq \theta_c \tag{21}$$

V.C.3. Implementation

During the propagation of the trajectory, the propagation obtains an optimal control trajectory for the remainder of the trajectory at frequency of 0.5 Hz. This optimal control is predicted using GPOPS, a pseudospectral optimal control software.[25–29] In the case where the range is to be maximized, the objective function used in GPOPS is given by

$$\mathcal{J} = -s_f = -s(t_f) \tag{22}$$

Similarly, when the accuracy is to be maximized, the objective function is given as

$$\mathcal{J} = d^2_{miss} = \left(\mathbf{r}(t_f) - \mathbf{r_T}\right)^T \left(\mathbf{r}(t_f) - \mathbf{r_T}\right) \tag{23}$$

which is equivalent to minimizing the miss distance.

V.D. Trajectory Analysis

The equations of motion for the system that are utilized are expressed in terms of their Cartesian coordinates as to eliminate singularities that can arise with the use of angles. The system dynamics are described by the relation

$$\begin{pmatrix} {}^{\mathcal{I}}\dfrac{d\mathbf{r}^{\mathcal{I}}}{dt} \\ {}^{\mathcal{I}}\dfrac{d\mathbf{v}^{\mathcal{I}}}{dt} \end{pmatrix}_{6\times 1} = \begin{pmatrix} \mathbf{v}^{\mathcal{I}} \\ \dfrac{1}{m}\sum \mathbf{f}^{\mathcal{I}} \end{pmatrix}_{6\times 1} \tag{24}$$

In Eq. (24), the vectors are all expressed in the inertial frame ($\mathcal{I}$) and the derivatives are taken with respect to the inertial frame. Therefore, all of the forces acting on the entry system need to be expressed in the inertial frame. For instance, the force due to drag is most easily expressed in the body-frame and thus needs transformation into the inertial frame. This is done using a transformation matrix approach seen in Eq. (25) where $\mathbf{L_{BA}}$ is the transformation matrix from Frame $\mathcal{A}$ to Frame $\mathcal{B}$, $\boldsymbol{\xi}^{\mathcal{A}}$ is an arbitrary vector expressed in Frame $\mathcal{A}$, and $\boldsymbol{\xi}^{\mathcal{B}}$ is the same arbitrary vector expressed in Frame $\mathcal{B}$.

$$\boldsymbol{\xi}^{\mathcal{B}} = \mathbf{L_{BA}}\boldsymbol{\xi}^{\mathcal{A}} \tag{25}$$

The transformation matrix, $\mathbf{L_{BA}}$, is given by

$$\mathbf{L_{BA}} = \begin{pmatrix} \mathbf{i}^{\mathcal{B}} \cdot \mathbf{i}^{\mathcal{A}} & \mathbf{i}^{\mathcal{B}} \cdot \mathbf{j}^{\mathcal{A}} & \mathbf{i}^{\mathcal{B}} \cdot \mathbf{k}^{\mathcal{A}} \\ \mathbf{j}^{\mathcal{B}} \cdot \mathbf{i}^{\mathcal{A}} & \mathbf{j}^{\mathcal{B}} \cdot \mathbf{j}^{\mathcal{A}} & \mathbf{j}^{\mathcal{B}} \cdot \mathbf{k}^{\mathcal{A}} \\ \mathbf{k}^{\mathcal{B}} \cdot \mathbf{i}^{\mathcal{A}} & \mathbf{k}^{\mathcal{B}} \cdot \mathbf{j}^{\mathcal{A}} & \mathbf{k}^{\mathcal{B}} \cdot \mathbf{k}^{\mathcal{A}} \end{pmatrix} \tag{26}$$

where it is assumed that the vectors in Frame $\mathcal{A}$ have the form $\boldsymbol{\xi}^{\mathcal{A}} = \xi_x \mathbf{i}^{\mathcal{A}} + \xi_y \mathbf{j}^{\mathcal{A}} + \xi_z \mathbf{k}^{\mathcal{A}}$ and the vectors in Frame $\mathcal{B}$ have the form $\boldsymbol{\xi}^{\mathcal{B}} = \xi_x \mathbf{i}^{\mathcal{B}} + \xi_y \mathbf{j}^{\mathcal{B}} + \xi_z \mathbf{k}^{\mathcal{B}}$.

There are three primary forces acting on the body—weight, $\mathbf{W}$, lift, $\mathbf{L}$, and drag, $\mathbf{D}$. The lift vector is dashed because it is is the projection into the velocity of force. There is an additional component associated with this force that could be out-of-plane. The weight vector, $\mathbf{W}$, is expressed as

$$\mathbf{W} = m\mathbf{g} \tag{27}$$

The lift vector's magnitude is give as

$$L = \frac{1}{2}\rho \parallel \mathbf{v}_{\text{rel}} \parallel^2 C_L S \tag{28}$$

The lift vector is perpendicular to the relative velocity vector is composed of a composition of two rotations—one rotation about the velocity vector by angle σ, followed by a 90° rotation about the vehicle's angular momentum vector. Finally the drag vector, $\mathbf{D}$, is given by

$$\mathbf{D} = -\frac{1}{2}\rho \parallel \mathbf{v}_{\text{rel}} \parallel^2 C_D S \frac{\mathbf{v}_{\text{rel}}}{\parallel \mathbf{v}_{\text{rel}} \parallel} \tag{29}$$

In addition to the Cartesian equations of motion in Eq. (24), an additional equation for the range of the system is also propagated. This equation for the range is given by

$$\dot{s} = v\cos(\gamma) \tag{30}$$

These equations were propagated from the initial state using a fixed-step RK-4 propagator until the vehicle reached the surface (*i.e.*, $h = 0$). The output of this CA passed to other CAs is the trajectory as a function of time.

V.E. Thermal Response

A Sutton-Graves approximation for the stagnation point heating on the system is used.

$$\dot{q}_s = k_s \sqrt{\frac{\rho}{r_n}} v^3 \tag{31}$$

In this case, the stagnation point is taken to be the leading edge of the deployable such that $r_n = 0.25$ m and the nominal value of the Sutton-Graves constant, k_s, is 1.74153×10^{-4} $\text{kg}^{1/2}\text{m}^{-1/2}$.

V.F. Weights and Sizing

V.F.1. Deployable Structure

The sizing of the deployable's structure is based on work by Krivoshapko for ellipsoidal shell pressure vessels where analytical relationships for the meridional and parallel stresses and critical buckling pressure are given in terms of the geometry of the ellipse.[30]

$$\sigma_\phi = \frac{p}{2b\delta}\sqrt{r^2(b^2 - a^2) + a^4} \tag{32}$$

$$\sigma_\beta = \frac{p}{2b\delta}\frac{2r^2(b^2 - a^2) + a^4}{\sqrt{r^2(b^2 - a^2) + a^4}} \tag{33}$$

$$p_{cr} = \frac{16E\delta^4}{a^2\sqrt{3(1-\nu^2)}}\left[1 + \left(\frac{z}{a}\right)^{1/2}\sqrt{\frac{193(1-4\delta^2)}{16\delta\sqrt{12(1-\nu^2)}}}\right] \tag{34}$$

In this work, the thickness, δ, is chosen based on minimum thickness resulting from Eqs. (32), (33), and (34) when a factor of safety of 1.3 is applied. The value of the internal pressure, p, is chosen such that it is twice the maximum dynamic pressure experienced. The dimensions of the ellipsoid are such that it is the minimum volume that encompasses the deployable. The deployable's mass is determined by the following relationship

$$m_{structure} = \frac{3lz\delta}{4}\sqrt{3l^2}\rho_d \tag{35}$$

which accounts for an increase in mass of 50% to account for deployable systems and design immaturity.

V.F.2. Deployable TPS System

A first-order relationship determined by Laub and Venkatapathy uses heat load as the sole parameter to determine the thermal protection system (TPS) mass fraction.[31] This approximate relation is used in this investigation to size the TPS material for the deployable. The model uses historical United States planetary missions at Venus, Earth, Mars, and Jupiter with ablative TPS to regress TPS mass fraction against the integrated heat load. These missions have integrated heat loads ranging from approximately 3×10^3 J/cm^2 to 2×10^5 J/cm^2 (the trajectories analyzed in this investigation have heat loads that are approximately 7-12 $\times 10^3$ J/cm^2). The derived mass model for the TPS is given by[31]

$$m_{TPS} = \left(9.1 \times 10^{-4} Q^{0.51575}\right) m_0 \tag{36}$$

where Q is the integrated heat load in J/cm^2 and m_0 is the entry mass.

V.F.3. Deployable Mass

The total deployable's mass is the addition of the structural mass and the TPS system.

$$m_{deploy} = m_{structure} + m_{TPS} \tag{37}$$

VI. Results and Discussion

VI.A. Design Parameters

The solutions presented subsequently are based on the deterministic and probabilistic parameters shown in Table 1. These represent the inputs into the various models in order to actually complete the design process. The values listed are consistent with the assumptions stated previously, with atmospheric parameters based on typical Earth values, trajectory values are typical values for the burnout state of a strategic vehicle on a depressed trajectory, heating parameters consistent with the Sutton-Graves model, and material properties similar to that of Dacron.[32–34]

VI.B. Design Constraints

Several practical design constraints exist in this design space. These include:

1. A limitation on the size of the deployable: $l/d \in [0.0, 2.0]$
2. A limitation on the mass of the deployable: $m_{deploy} \leq 5,000$ kg
3. A restriction that the range must be greater than the range with no deployable: $s_f \geq s_{f,baseline}$
4. A restriction that the accuracy must be greater than the accuracy with no deployable: $d_{miss} \leq d_{miss,baseline}$
5. A restriction that the heating must be consistent with anticipated deployable ablative TPS materials: $\dot{q}_s \leq 100$ W/cm^2

Each of these constraints are appended to the objective function as discussed in Ref. 35.

Table 1. Parameter values for the design.

Parameter	Description	Nominal Value	Distribution
μ_g	Gravitational Parameter	3.986×10^5 km^3/m^2	$\mathcal{N}(3.986 \times 10^5, 10^6)$
ρ_0	Surface Atmospheric Density	1.225 kg/m^3	$\mathcal{N}(1.225, 0.01)$
H	Scale Height	7.116 km	$\mathcal{N}(7.116, 4)$
k_{C_L}	Lift Coefficient Multiplier	1	$\mathcal{N}(1, 0.0625)$
k_{C_D}	Drag Coefficient Multiplier	1	$\mathcal{N}(1, 0.0625)$
m_0	Initial Mass	5,000 kg	—
h_0	Initial Altitude	155 km	—
v_0	Initial Velocity Magnitude	6,200 m/s	$\mathcal{N}(6200, 40000)$
γ_0	Initial Flight Path Angle	$-9.6°$	$\mathcal{N}(-9.6, 0.04)$
θ_0	Initial Latitude	Design Variable	$\mathcal{N}(\theta_0, 0.0625)$
ϕ_0	Initial Longitude	Design Variable	$\mathcal{N}(\phi_0, 0.0625)$
ψ_0	Initial Heading Angle	90°	$\mathcal{N}(90, 4)$
h_T	Target Altitude	0 m	—
ϕ_T	Target Longitude	0°	—
θ_T	Target Latitude	10.354°	—
k_s	Sutton-Graves Constant	$1.74153 \times 10^{-4}\ \sqrt{\frac{\text{kg}}{\text{m}}}$	$\mathcal{N}(1.74153 \times 10^{-4}, 1 \times 10^{-8})$
r_n	Stagnation Radius	0.25 m	$\mathcal{N}(0.25, 0.0025)$
ρ_d	Deployable Material Density	1.3 g/cm^2	$\mathcal{N}(1.3, 0.01)$
E	Deployable Young's Modulus	3,000 MPa	$\mathcal{N}(3000, 90000)$
σ_t	Deployable Strength	60 MPa	$\mathcal{N}(60, 100)$
ν	Deployable Poisson Ratio	0.4	—

VI.C. Standard Form of the Optimization Problem

The optimization problem, in standard form, is given by

$$\left.\begin{array}{ll} \textbf{Minimize}: & [\mathcal{J}_{mass} \quad -\mathcal{J}_{range}] \text{ or } [\mathcal{J}_{mass} \quad \mathcal{J}_{accuracy}] \\ \textbf{Subject to}: & g_1(l/d, \theta_0, \phi_0) = -l/d \leq 0 \\ & g_2(l/d, \theta_0, \phi_0) = l/d \leq 2 \\ & g_3(l/d, \theta_0, \phi_0) = m_{deploy}(l/d) - 5000 \leq 0 \\ & g_4(l/d, \theta_0, \phi_0) = s_{f,baseline} - s_f(l/d) \leq 0 \\ & g_5(l/d, \theta_0, \phi_0) = d_{miss}(l/d, \theta_0, \phi_0) - d_{miss,baseline} \leq 0 \\ & g_6(l/d, \theta_0, \phi_0) = \dot{q}_s(l/d) - 100 \leq 0 \\ \textbf{By varying}: & l/d, \theta_0, \phi_0 \end{array}\right\}$$

where

$$\mathcal{J}_{mass} = \frac{\bar{m}_{deploy}}{m_0} + \frac{\sigma^2_{m_{deploy}}}{m_0^2}$$

$$\mathcal{J}_{range} = \frac{\bar{s_f}}{s_{f,baseline}} - \frac{\sigma^2_{s_f}}{s^2_{f,baseline}}$$

$$\mathcal{J}_{accuracy} = \frac{\bar{d}_{miss}}{d_{miss,baseline}} + \frac{\sigma^2_{d_{miss}}}{d^2_{miss,baseline}}$$

In terms of the rapid robust design methodology, the quantity $\frac{\sigma_x^2}{x^2}$ can be replaced with $\frac{\| \mathbf{\Sigma}_{\boldsymbol{y}^*_{\boldsymbol{x}}} \|_2}{x^2}$ for the quantity x.

VI.D. Single-Delta Design Solutions

Converged, optimal deployable designs for the single-delta configuration shown in Fig. 5 are shown in Figs. 6 and 7. The points in blue corresponding the rapid robust multidisciplinary design methodology and points

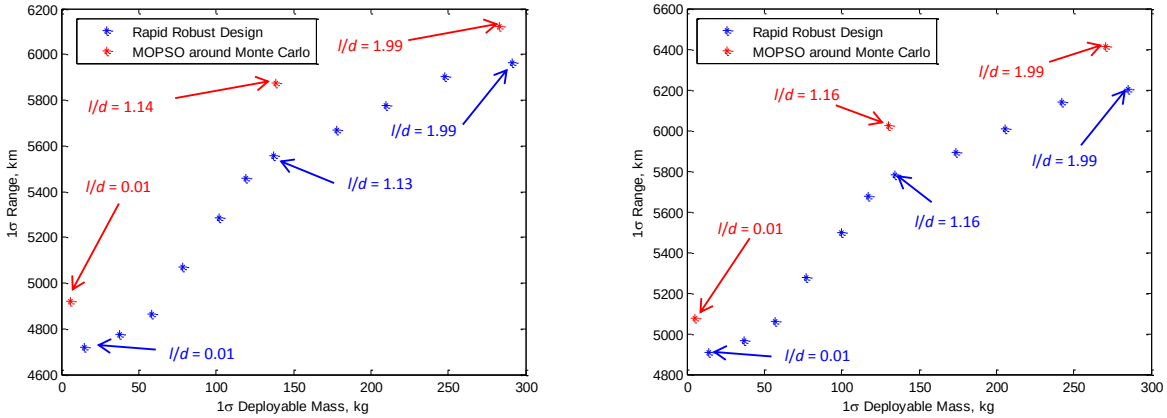

(a) (b)

Figure 6. Design solutions for range comparing the rapid robust design methodology and a multiobjective particle swarm optimizer for a (a) bank-to-steer guidance algorithm and the (b) acceleration control guidance algorithm.

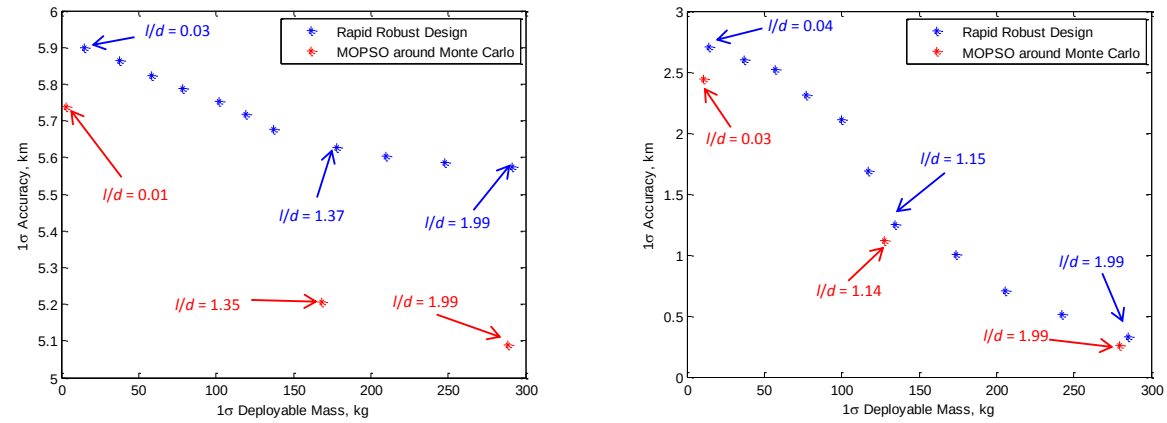

(a) (b)

Figure 7. Design solutions for accuracy comparing the rapid robust design methodology and a multiobjective particle swarm optimizer for a (a) bank-to-steer guidance algorithm and the (b) acceleration control guidance algorithm.

in red corresponding to designs optimal by using a multi-objective particle swarm optimizer (MOPSO) wrapped around a Monte Carlo simulation.

Correlation between the MOPSO results and those obtained through the rapid robust design methodology is seen in both Figs. 6 and 7. The discrepancy in values can be attributed the conservatism provided by the bounding technique on the variance estimates in the rapid robust design methodology, since the variance value used is the largest eigenvalue of the propagated covariance matrix.

Figure 6 demonstrates that the larger the deployable's mass, the more range that the strategic system will have. In fact, for an approximately 300 kg deployable, the range is improved over 1,200 km (an improvement of greater than 25%). The range is seen insensitive to the two guidance algorithms considered. This is due to the fact the trajectory for maximum range is largely a full-lift up trajectory which is equally capable of being flown by a bank-to-steer algorithm and the acceleration control method. For an equally weighted objective function between range and mass, the optimal design has a l/d of 1.16 ($m_{deploy} = 139$ kg), regadless of the guidance algorithm.

Figure 7 demonstrates that the larger the deployable is, the more accurate the system will be. For an

approximately 300 kg deployable, the accuracy is capable of being improved by an order of magnitude from the baseline strategic system (from 2.8 km to 0.3 km). Unlike the range, the accuracy of the system is very sensitive to the guidance algorithm. For the bank-to-steer algorithm, the control is nearly saturated with a miss distance of about 5.5 km across all deployable sizes. However, using acceleration control, improvement is consistently seen with a larger deployables (with larger L/D). For an equally weighted objective function between range and mass using acceleration control, the optimal design has a l/d of 1.14 ($m_{deploy} = 131$ kg).

A significant advantage of the rapid robust design methodology is computational runtime. This is shown in Table 2 where the number of iterations required to obtain the results shown in Figs. 6 and 7 is provided.

Table 2. Computational comparison between MOPSO and the Rapid Robust Design Methodology.

	Range		**Accuracy**	
	Rapid Robust Design Methodology	*MOPSO*	*Rapid Robust Design Methodology*	*MOPSO*
Number of DSM Iterations, -	24,962	560,684	28,616	600,004
Computational Runtime, hours	2.2	49.8	2.4	57.3

The MOPSO results were the result of propagating 1,000 Monte Carlo samples. Despite returning approximately four times as many solutions as the MOPSO approach, the number of analysis iterations of the rapid robust design methodology is an order of magnitude less with runtimes less than 5% that of the MOPSO. In addition, the probabilistic results obtained by this new methodology are within 10% of those obtained using the MOPSO, with the vast majority having errors less than 3% the MOPSO values.

VI.E. Center of Gravity Considerations

The results presented thus far allow for the center of gravity (CG) to be positioned anywhere, including outside of the outer mold line of the vehicle. This is not practical. As shown in Fig. 8, when limiting the CG to be within the vehicle, the maximum L/D achievable diminishes to a point where it is actually less than the baseline system.

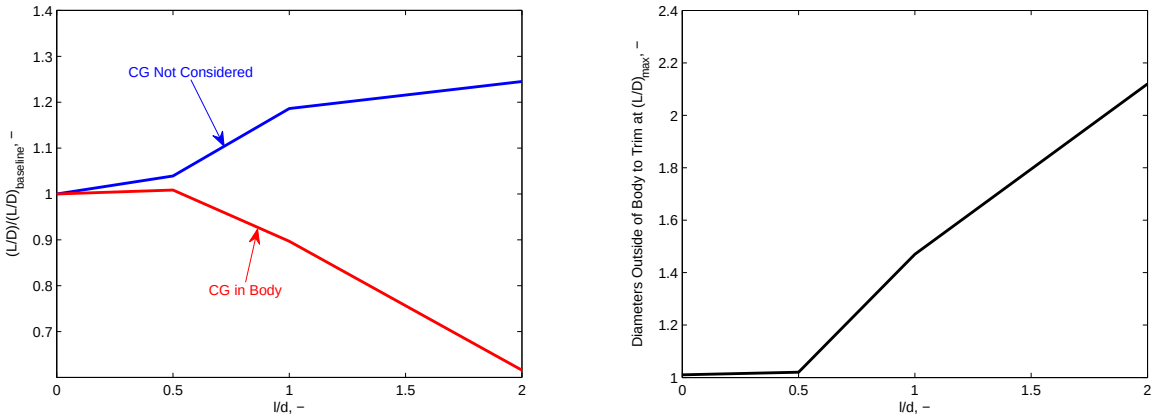

(a) (b)

Figure 8. The (a) impact on L/D of constraining the CG position to be within the vehicle and (b) the normalized (relative to the vehicle's diameter) distance outside the vehicle the CG needs to be to achieve $(L/D)_{\max}$.

In order to achieve trim conditions, a body flap was added to the baseline system. This body flap was assumed to be a flat surface that was 25% of the vehicle's length. Figure 9 shows that the body flap deflection angle in order to achieve the maximum L/D achievable. Note that the deflection angle remains less than 30° for all deployable sizes considered.

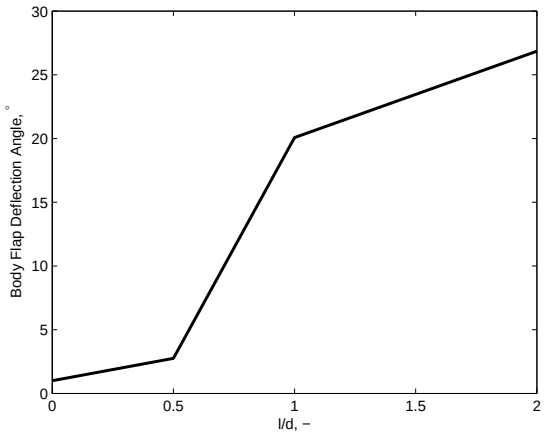

Figure 9. Body flap deflection angle required to trim the vehicle at the theoretical maximum L/D.

VI.F. Alternative Configuration

An additional deployable configurations were assessed to identify whether an improvement in L/D can be obtained without the inclusion of a body flap. This configuration is shown in Fig. 10.

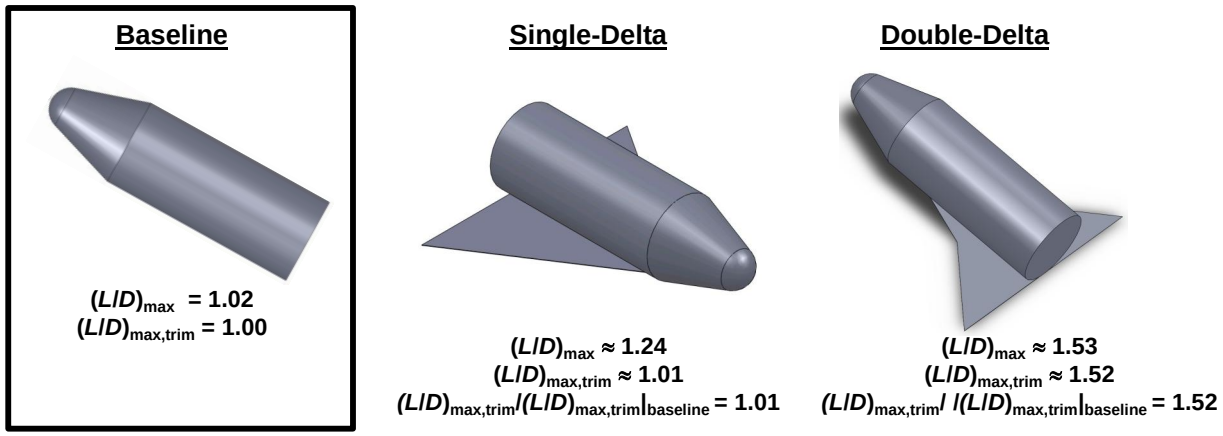

Figure 10. Comparison of investigated deployable concepts showing the maximum achievable L/D accounting for trim considerations.

While the single-delta deployable concept previously described does not provide improvement in performance without the addition of a body flap, the double-delta configuration provides a significant increase in L/D (52%) relative to the baseline strategic vehicle. The large performance improvement of the double-delta configuration without the use of a body flap can be explained by the aerodynamic force of the deployable being located farther aft than in the single-delta concept. The mean aerodynamic center of the baseline vehicle is located close to the cylinder cap beneath the nose cone. The lift of the double-delta deployable is sufficiently far aft to provide an a sufficient restoring momement to allow the vehicle to trim, whereas this is not the case for the single-delta configuration. It should also be noted, however, that for the double-delta, the CG to trim at L/D_{max} shifts aft as l/d increases resulting in the vehicle losing the ability to trim as l/d increases (however, for $l/d \leq 2.0$ this effect was not observed).

The trim angle of attack for these vehicles is significant ($\sim 20°$), which allows for another advantageous feature of the double-delta relative to single-delta to be exploited—less drag area. This enables a larger L/D increase relative to the single-delta configuration discussed previously. However, this is traded for a more complex shape which would be significantly more difficult to manufacture and deploy in flight.

VI.G. Double Delta Design Solutions

Converged, optimal double-delta deployable designs are shown in Figs. 11 and 12.

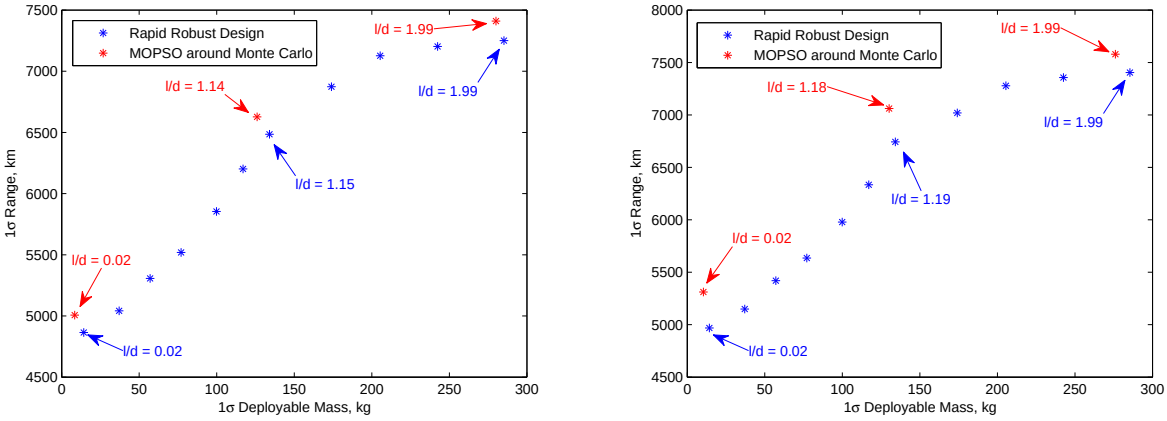

(a) (b)

Figure 11. Design solutions for range comparing the rapid robust design methodology and a multiobjective particle swarm optimizer for a (a) bank-to-steer guidance algorithm and the (b) acceleration control guidance algorithm for the double-delta configuration.

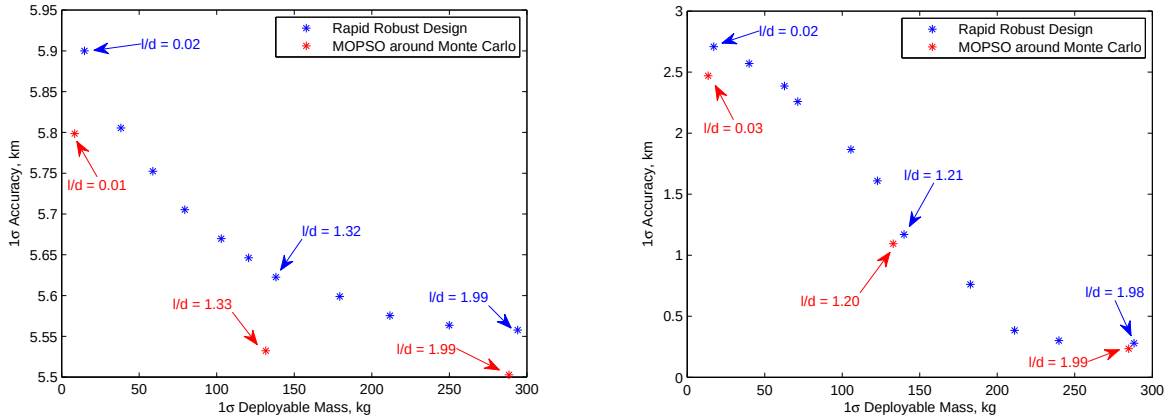

(a) (b)

Figure 12. Design solutions for accuracy comparing the rapid robust design methodology and a multiobjective particle swarm optimizer for a (a) bank-to-steer guidance algorithm and the (b) acceleration control guidance algorithm for the double-delta deployable.

As before, there is strong correlation between the MOPSO results and those obtained through this methodology. However, in this case, as shown in Fig. 11, the range performance is significantly improved for larger deployables. For an approximately 300 kg deployable, the range is improved over 2,400 km (an improvement that is twice that of the single-delta with a body flap configuration). Furthermore, the insensitivity to guidance algorithm is persistent in the double-delta configuration, since the trajectory is again largely full-lift up. For an equally weighted objective function between range and mass, the optimal design has a l/d of 1.19, regardless of the guidance algorithm ($m_{deploy} = 148$ kg).

Figure 12 for the double-delta shows similar trends to the single-delta configuration—the larger the deployable is, the more accurate the system will be. When considering accuracy, however, the performance gains of the double-delta configuration is not as great compared to range benefits. For an approximately 300 kg deployable, the accuracy is 0.2 km for the double-delta configuration, compared to 0.3 km for the single-delta. This is a marginal improvement for the double-delta configuration relative to the single-delta with a body flap configuration. However, the rate of improving accuracy as the deployable increases in size (from an l/d of 0 to l/d of 2.0) is faster compared to the single-delta and a body flap is not required in order to achieve

these performance gains. Again, the accuracy of the system is very sensitive to the guidance algorithm, with the bank-to-steer guidance demonstrating saturated qualities. For an equally weighted objective function between range and mass using acceleration control, the optimal design has a l/d of 1.2 ($m_{deploy} = 149$ kg).

The computational runtime advantage of the rapid robust design methodology is shown in Table 3 where accuracies acceptable to conceptual design are shown to be achievable.

Table 3. Computational comparison between MOPSO and the Rapid Robust Design Methodology.

	Range		**Accuracy**	
	Rapid Robust Design Methodology	*MOPSO*	*Rapid Robust Design Methodology*	*MOPSO*
Number of DSM Iterations, -	26,842	642,132	33,534	713,124
Computational Runtime, hours	2.3	59.6	2.8	64.2

VII. Conclusions

A rapid robust design methodology was implemented to perform the rapid design of a deployable system for a strategic system with the objective to either increase the range of the system or the accuracy of the system. The rapid robust design methodology was shown to provide similar results to a MOPSO wrapped around a Monte Carlo with solutions within 10% of the MOPSO solutions for less than 5% of the computational time.

Two deployable configurations were investigated—a single-delta and a double-delta. For a 300 kg deployable, the single-delta configuration was shown to provide an increase in 1σ range of more than 1,200 km (25%) and a reduction in 1σ miss distance from 2.5 km to 0.5 km (500%) over the baseline strategic system. However, when requiring the CG of the vehicle to be within the baseline strategic system's outer mold line, a body flap is required to achieve any performance gains. On the other hand, a 300 kg double-delta is able to increase the baseline system's 1σ range by over 2,400 km (50%) and reduce the 1σ miss distance by an order of magnitude (to less than 0.25 km) without the use of a body flap.

In addition to configuration, the effect of guidance algorithm was investigated using a bank-to-steer algorithm and a bounding guidance algorithm. The range results were insensitive to the varying guidance algorithms as the trajectories were largely full-lift up. However, when accuracy is considered, the guidance algorithm was shown to have a large effect as the bank-to-steer algorithm's control was shown to be nearly saturated with marginal performance gains across the deployable sizes investigated.

Acknowledgments

This work was performed under a Charles Stark Draper Laboratory URaD entitled "An Investigation of Guidance, Control, and Mission Design Implications of Hypersonic Deployable Aerodynamic Devices." The authors would like to thank Zach Putnam and Ian Meginnis for their insight into the formulation of the problem described within this paper.

References

[1]Gates, K. L., McRonald, A. D., Nock, K. T., and Aaron, K. M., "Trading Robustness Requirements in Mars Entry Trajectory Design," *AIAA 2010-7974*, Toronto, Ontario, Canada, Aug. 2010.

[2]Lu, F. K., Hyungwon, K., and McNay, L. N., "A Simplified Trajectory Analysis Model for Small Satellite Payload Recovery from Low Earth Orbit," *Aerospace Science and Technology*, Vol. 7, No. 3, 2003.

[3]Bloetscher, F. and Pinnell, W. R., "Correlation of Analytical and Empirical Techniques for Designing Supersonic and Hypersonic Decelerators," *AIAA 1966-1517*, 1966.

[4]Dwyer-Cianciolo, A. M., Davis, J. L., Komar, D. R., Munk, M. M., Samareh, J. A., Powell, R. W., Shidner, J. D., Stanley, D. O., Wilhite, A. W., Kinney, D. J., McGuire, M. K., Arnold, J. O., Howard, A. R., Sostaric, R. R., Studak, J. W., Zumwalt, C. H., Llama, E. G., Casoliva, J., Ivanov, M. C., Clark, I., and Sengupta, A., "Entry, Descent and Landing Systems Analysis Study: Phase 1 Report," Tech. Rep. TM-2010-216720, NASA, July 2010.

[5]Brown, G. J., Lingard, J. S., Darley, M. G., and Underwood, J. C., "Aerocapture Decelerators for Mars Orbiters," *AIAA 2007-2543*, Williamsburg, VA, May 2007.

[6]Jaremenko, I., "BALLUTE Characteristics in the 0.1 to 10 Mach Number Speed Regime," *Journal of Spacecraft and Rockets*, Vol. 4, No. 8, 1967.

[7]Pepper, W. B., "Development of a Composite Structure Hypersonic Parachute," *Journal of Spacecraft and Rockets*, Vol. 6, No. 4, 1969.

[8]Kyser, A. C., "The Rotornet: A High-Performance Hypersonic Decelerator for Planetary Entry," Tech. Rep. CR-247, NASA, June 1965.

[9]Trabandt, U., Koeler, H., and Schmid, M., "Deployable CMC Hot Structure Decelerator for Aerobrake," *AIAA 2003-2169*, Monterey, CA, May 2003.

[10]Green, M. J., Swenson, B. L., and Balakrishnan, A., "Aerothermodynamic Environment for a Titan Probe with Deployable Decelerator," *AIAA 1985-1063*, Williamsburg, VA, June 1985.

[11]Venkatapathy, E., Arnold, J., Fernandez, I., Kenneth R. Hamm, J., Kinney, D., Laub, B., Makino, A., McGuire, M. K., Peterson, K., Prabhu, D., Empey, D., Dupzyk, I., Huynh, L., Hajela, P., Gage, P., Howard, A., and Andrews, D., "Adaptive Deployable Entry and Placement Technology (ADEPT): A Feasibility Study for Human Missions to Mars," *AIAA 2011-2608*, Dublin, Ireland, May 2011.

[12]Horvath, T. J., ., T. F. O., Cheatwood, F. M., Prabhu, R. K., and Alter, S. J., "Experimental Hypersonic Aerodynamic Characteristics of the 2001 Mars Surveyor Precision Lander with Flap," *AIAA 2002-4408*, Monterey, CA, Aug. 2002.

[13]Lockwood, M. K., Powell, R. W., Sutton, K., Prabhu, R. K., Graves, C. A., Epp, C. D., and Carman, G. L., "Entry Configurations and Performance Comparisons for the Mars SMART Lander," *Journal of Spacecraft and Rockets*, Vol. 43, No. 2, 2006.

[14]Wilhite, A. W., Bush, L. B., Cruz, C. I., Lepsch, R. A., Morris, W. D., Stanley, D. O., and Wurster, K. E., "Advanced Technologies for Rocket Single State to Orbit Vehicles," *Journal of Spacecraft and Rockets*, Vol. 28, No. 6, 1991.

[15]Capricci, M., "European Crew and Logistics Vehicles for ISS and Exploration Missions," *AIAA 2005-3252*, Capua, Italy, May 2005.

[16]Allen, H. J. and A. J. Eggers, J., "A Study of the Motion and Aerodynamic Heating of Ballistic Missiles Entering the Earth's Atmosphere at High Supersonic Speeds," Tech. Rep. 1381, NACA, 1957.

[17]Steinfeldt, B. A. and Braun, R. D., "Utilizing Dynamical Systems Concepts in Multidisciplinary Design," *AIAA 2012-5655*, Indianapolis, IN, Sept. 2012.

[18]Steinfeldt, B. A. and Braun, R. D., "Design Covergence Using Stability Concepts from Dynamical Systems Theory," *AIAA 2012-5657*, Indianapolis, IN, Sept. 2012.

[19]Julier, S. J. and Uhlmann, J. K., "A General Method for Approximating Nonlinear Transformations of Proability Distributions," Tech. rep., University of Oxford, Nov. 1996.

[20]Khalil, H. K., *Nonlinear Systems, 3rd Ed.*, Prentice Hall, 2002.

[21]Papachristodoulou, A. and Prajna, S., "On the Construction of Lyapunov Functions using the Sum of Squares Decomposition," *Proceedings of the 41st IEEE Conference on Decision and Control*, Piscatway, NJ, Dec. 2002.

[22]Kinney, D. J., "Aero-Thermodynamics for Conceptual Design," *AIAA 2004-13382, 2004 AIAA Aerospace Sciences Meeting and Exhibit*, Reno, NV, Jan. 2004.

[23]"The Apollo Entry Guidance: A Review of the Mathematical Development and Its Operational Characteristics," Tech. Rep. T75-14618, NASA, 1969.

[24]Mendeck, G. F. and Craig, L. E., "Entry Guidance for the 2011 Mars Science Laboratory mission," *AIAA 2011-6639*, Portland, OR, Aug. 2011.

[25]Rao, A. V., Benson, D. A., Darby, C. L., Patterson, M. A., Francolin., C., Sanders, I., and Huntington, G. T., "Algorithm 902: GPOPS, A MATLAB Software for Solving Multiple-Phase Optimal Control Problems Using the Gauss Psuedospectral Method," *ACM Transactions on Mathematical Software*, Vol. 37, No. 2, 2010.

[26]Benson, D. A., Huntington, G. T., Thorvaldsen, T. P., and Rao, A. V., "Direct Trajectory Optimization and Costate Estimation via an Orthogonal Collocation Method," *Journal of Guidance, Control, and Dynamics*, Vol. 29, No. 6, 2006.

[27]Garg, D., Patterson, M. A., Darby, C. L., Francolin, C., Huntington, G. T., Hager, W. W., and Rao, A. V., "Direct Trajectory Optimization and Costate Estimation of Finite-Horizon and Infinite-Horizon Optimal Control Problems Using a Radau Pseudospectral Method," *Computational Optimization and Applications*, Vol. 49, No. 2, 2011.

[28]Garg, D., Patterson, M. A., Hager, W. W., Rao, A. V., Benson, D. A., and Huntington, G. T., "A Unified Framework for the Numerical Solution of Optimal Control Problems Using Pseudospectral Methods," *Automatica*, Vol. 46, No. 11, 2010.

[29]Garg, D., Hager, W. W., and Rao, A. V., "Pseudospectral Methods for Solving Infinite-Horizon Optimal Control Problems," *Automatica*, Vol. 47, No. 4, 2011.

[30]Krivoshapko, S. N., "Research on General and Axisymmetric Ellipsoidal Shells Used as Domes, Pressure Vessels, and Tanks," *Journal of Applied Mechanics*, Vol. 60, No. 6, 2008.

[31]Laub, B. and Venkatapathy, E., "Thermal Protection System Technology and Facility Needs for Demanding Future Planetary Missions," *International Workshop on Planetary Probe Atmospheric Entry and Descent Trajectory Analysis and Science Proceedings*, Lisbon, Portugal, Oct. 2003.

[32]Gronlund, K. and Wright, D. C., "Depressed Trajectory SLBMs: A Technical Evaluation and Arms Control Possibilities," *Science & Global Security*, Vol. 3, 1992.

[33]Sutton, K. and Graves, R. A., "A General Stagnation-Point Convective-Heating Equation for Arbitrary Gas Mixtures," Tech. Rep. TR-R-376, NASA, 1971.

[34]Spence, D. C., "Effects of a Simulated Martian Mission on the Mechanical Properties of Dacron Parachute Material," Tech. Rep. TN D-6242, NASA, 1971.

[35]Steinfeldt, B. A. and Braun, R. D., "Leveraging Dynamical Systems Theory to Incorporate Design Constraints for Multidisciplinary Design Problems," *51st AIAA Aerospace Sciences Meeting including the New Horizos Forum and Aerospace Exposition*, Grapevine, TX, Jan. 2013.